Design and feasibility testing of a high resolution, 3D printer using concentrated solar power

Böhmer, T.S.[a], Sonnendecker, P.W.[a] and Badenhorst, H.[a,b*]

[a] *University of Pretoria, Department of Chemical Engineering, Lynnwood Road, Pretoria, South Africa, 0083*

[b] *The University of Manchester, School of Chemical Engineering & Analytical Science, The Mill, Sackville Street, Manchester, United Kingdom, M1 3AL*

Highlights

• A novel method for 3D printing of commercial SLS powder using concentrated solar power.

• Approach uses a Fresnel lens and new heliostat design.

• Testing completed on commercial Nylon 12 powder and solar salt.

• Limits for operation and process model identified with layer thicknesses of 0.3 mm.

• Approach is feasible for printing with sunlight by developing suitable control system.

Abstract

Additive manufacturing (3D printing), combined with computer aided design, is transforming the modern manufacturing industry. Using high temperature techniques such as “selective laser sintering”, fabricators are given access to a wide range of starting materials. The sustainability of the approach could be improved through the direct use of concentrated sunlight to sinter these powders. Using inexpensive components, the cost can also be decreased to enable utilization by microbusinesses, especially those operating in remote, off-grid locations. For achieving this goal a high resolution prototype has been developed and constructed using a Fresnel lens design. To determine the feasibility of the method, two

dimensional sintering tests were conducted on a commercial Nylon 12 powder. The effects of the most influential parameters on this process were determined through the implementation of a simplified model and dimensional analysis.

The most important parameter for the description of the process was found to be the dimensionless ratio of incoming radiative power to power required for sintering or melting. For conditions in which only a single phase transformation takes place, this parameter was found to remain constant, with a mean of 6.84 and variance of 0.04. The limits of the power to speed ratio were also determined, achieving thicknesses as low as 0.3 mm for the selected powder and lens combination. The measured parameters demonstrate the feasibility of high resolution 3D printing using the proposed technique, provided that tailored control strategies are developed. A major limitation was found to be the focal spot size of the lens, which determines the track width. This can be improved from the current value of 3 mm through the use of a cast glass lens.

Keywords: additive manufacturing, concentrated solar energy, selective sintering

1. Introduction

Additive manufacturing, more commonly known as 3D printing, has revolutionized the manufacturing of functional components in a wide range of industries. The approach constructs three dimensional objects, layer by layer, using an electronic design file. The technique is fundamentally different from prior approaches which use “subtractive” machining, such as CNC milling or lathe turning, to shape parts by removing material. These techniques are limited in the geometries that can be produced, because the cutting tool cannot reach the interior of the starting block without carving out an access route. By instead constructing the component through the gradual addition of material in layers, they can be produced with very complex interior structures which are not accessible from the outside of the finished part.

This innovation has widened the application of structural optimization techniques to the design process. Using computerized topology optimization, the interior structure of a part can be optimized to withstand the same load as a solid one, but at substantially reduced weight. This has been successfully applied to the development of several Airbus aircraft [1], leading to capital and operational cost savings. Furthermore, the approach can also be used to rapidly produce systems with very complex, moving parts, thereby significantly reducing the man-hours required for design and fabrication [2]. Recently, numerous innovations have been suggested [3], it has even been proposed to construct 3D printed buildings [4]. The combination of computer aided design with the flexibility of additive manufacturing, has led to a reduction in the raw material, expertise, time and waste costs of producing complex products.

A wide range of additive manufacturing techniques exist, depending on the chosen raw material. The technique which has made it into the consumer mainstream is known as fused filament fabrication or fused deposition modelling (FDM). In this approach a heated extrusion head is used to deposit small beads or streams of a thermoplastic, which hardens to form the layers. An alternative method, known as selective laser sintering (SLS) or selective laser melting (SLM), is used extensively for the rapid prototyping of metal parts [5]. The operating procedure is slightly different: a roller deposits a layer of powder onto a height adjustable platform. A laser beam scans over regions of the powder bed, heating the powder to its melting point and either sintering or fusing the particles together. The platform is lowered, a new layer of powder is deposited, and the procedure is repeated. Once completed the excess powder is removed and the part can be cleaned or polished if required.

These processes generally do not convert or degrade the feedstock. Thus, the product can be easily recycled by selecting a suitable starting material and then after service grinding the part into a powder for reuse. The process could be made fully sustainable by utilizing renewable solar energy as the power source. This would also enable small scale, rural utilization where access to electricity infrastructure is limited. It may be possible to drive an "off-the-shelf" FDM printer using photovoltaics (PV) and suitable power electronics. However, for laser-based production of high-density metal parts, the power consumption can be very high, reaching up to several kW [6-8]. For a typical polycrystalline PV, operating at efficiencies below 20%, this would require a sizeable array, even for small scale work. Instead, it is sensible to explore the capture and use of solar irradiation directly as thermal energy.

Furthermore, laser-based devices are currently prohibitively expensive for small scale use or hobbyist manufacturing. Thus, a new low-cost method is needed to reach the energy density required for high temperature melting and/or sintering. In so doing, entrepreneurs and microbusiness, especially in developing nations, are given access to a wide range of manufacturing materials, including metals and ceramics. This will lead to the formation of new cottage industries, thereby stimulating economic growth and creating jobs. Concentrated solar power offers a solution to both of these issues. Numerous options exist for amplifying the maximum of around 1 $kW.m^{-2}$ reaching the earth's surface [9]. The correct option must be selected to be compatible with the requirements of additive manufacturing. This includes considerations such as a moving particle bed, point focus for high resolution, absorptance, variable irradiation, ambient losses and issues relating to the use of a non-electrical source, such as switching on and off and regulating the power output.

The objective of this study was to design and test a preliminary system which uses sunlight to sinter or melt a suitable, commercially available SLS powder. The components were chosen to be affordable, "off-the-shelf" items, in order to keep the overall costs down. The work represents the first step in establishing the viability of an affordable, high resolution, solar additive manufacturing platform. To limit the fabrication complexity, the investigation was constrained to the production of two-dimensional artefacts. A commercial SLS powder, Nylon 12 was selected as the test material for easy comparison to current laser-based units. To develop an understanding of the operating parameters, initial testing involved the variation of irradiance and scanning velocity to determine the impact on the produced layer thickness. A simplistic model for the process was developed and condensed to combinations of key parameters, or model functions, using dimensional analysis. The model was used to analyse the test data, in addition to the use of a second material, namely nitrate based solar salt ($NaNO_3$ - KNO_3). The salt provides a material with different thermal properties for robust validation. The developed relationship can be used to adjust the printer operation to

control layer thickness in the face of variable solar flux levels. The project aims to demonstrate that, despite some shortcomings compared to SLS, with further development 3D printing of a wide range of materials is feasible using selective solar sintering.

2. Design methodology

Numerous methods have been suggested for providing concentrated solar power. These can broadly be classified as line and point focus [9]. For additive manufacturing a small point source is needed, thus the former is not applicable. The achieved spot size controls the resolution of the print, which determines the smallest features that can be resolved by the technique. Two point-focus techniques are commonly utilized [10]: tower and dish. The solar power tower arrangement uses a collection of mirrors (heliostats) to reflect sunlight onto a central tower with a receiver. While this design is conceptually feasible, it would require a very complex tracking system and the achieved spot size would be limited by the size of the individual mirrors. As the mirror size is reduced the number would have to increase to maintain a given power output, making this a very expensive option. Parabolic dish concentrators function like conventional satellite dishes, focusing the sunlight onto a receiver located at the focal point, as demonstrated in Figure 1.

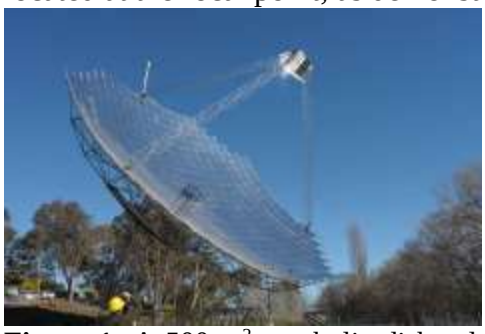

Figure 1: A 500 m^2 parabolic dish solar concentrator developed by Australian National University [11]

Both point focus techniques benefit from two-axis tracking, meaning the path of the sun is accurately followed to continuously reflect radiation on the focal point. Unfortunately, the focal point of the dish moves as the sun is tracked. This, in addition to the orientation of the collector, which is always away from the dish towards the sun, makes it very difficult to apply this technique to additive manufacturing. Not to mention that large parabolic dishes are expensive, requiring specialist equipment to manufacture. Fresnel lenses offer an inexpensive method for achieving very high solar concentration ratios [12]. These lenses are affordably manufactured by machining polycarbonate plastic. The design allows the construction of light-weight lenses, of large aperture and short focal length, without the mass and volume of material that would be required by a lens of conventional design, as shown in Figure 2.

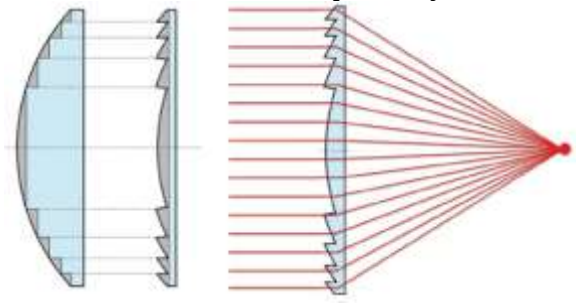

Figure 2: Fresnel lens design and operation

Past attempts to use Fresnel lenses have resulted in cumbersome tracking systems which direct the lens focal point onto a moving target [12-14] as depicted in Figure 3.

Figure 3: Fresnel lens based tracking systems [14]

These operate identically to the parabolic system with the exception that light is not reflected but transmitted and thus the focal point is on the opposite side, away from the sun. This design is feasible for use in a configuration similar to SLS, where the laser is scanned across the bed (Figure 4A). However, that would require that the entire tracking system with lens is continuously and precisely moved to position the focal spot at the point to be sintered/melted. An alternative configuration used in additive manufacturing, is to move the platform which holds the powder bed, while keeping the source stationary, as illustrated in Figure 4B. This is also possible, however, even with perfect tracking, the focal point of the lens, like the dish, is not stationary. Thus, the platform would have to undergo additional, complex adjustments to keep the focal point of the lens at the correct point on the bed. In this configuration the lens will generally also not be parallel to the bed, except for specific days at precisely noon. Thus, the focal spot would predominantly be an elliptical projection onto the bed, resulting in uneven heating. Despite these drawbacks, this configuration has been utilized to produce 3D printed artefacts [15-17]. The starting materials used comprise mainly coarse sand, resulting in very rough shapes, predominantly employed as artwork. Due to the issues mentioned, these systems cannot achieve the high resolution required for additive manufacturing.

Recently, numerous innovative concentrator designs have been proposed. Options such as total internal reflection collectors [18, 19] and the combination of prisms and lenses [20] can be used to significantly improve the optical efficiency of the system. Total internal reflection ensures maximum energy recovery, while the combined systems can achieve high concentration levels, permitting the attainment of very high temperatures. A particularly innovative concept is the use of fibre optic cables to redirect the concentrated light [21]. Since the cable is flexible it can be used to channel light from the focal point of parabolic dish concentrators to a fixed point in space. However, all of these designs add additional complexity and expense to the system, in most cases requiring components which are not readily available as “off-the-shelf”.

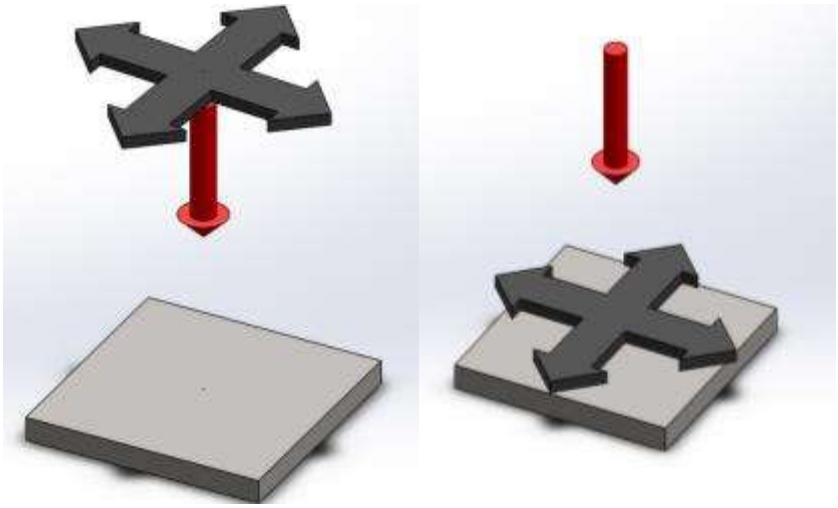

Figure 4: A) Moving energy/material source; B) Moving platform

In this investigation the solution to this problem was simply and inexpensively achieved by combining the solar power tower design with a Fresnel lens via a secondary mirror. The primary mirror (position 1 in Figure 5A) is a single heliostat which is equipped with two-axis tracking. The incoming radiation is redirected onto a stationary, secondary mirror (position 2) at an angle of 45º. This mirror reflects the light onto the Fresnel lens (position 3) which concentrates it to a fixed point in space. The platform is oriented in a North-South direction, facing North given its location in the southern hemisphere. When viewed from above, the primary mirror maintains an angle perpendicular to the direction given by the centreline of the angle between the sun and true North. In this way sunlight is reflected in a northerly direction throughout the day independent of the azimuth angle of the sun. The elevation of the sun is compensated for by adjusting the angle of this mirror with respect to the earth's horizontal surface. The operation is depicted schematically in Figure 5.

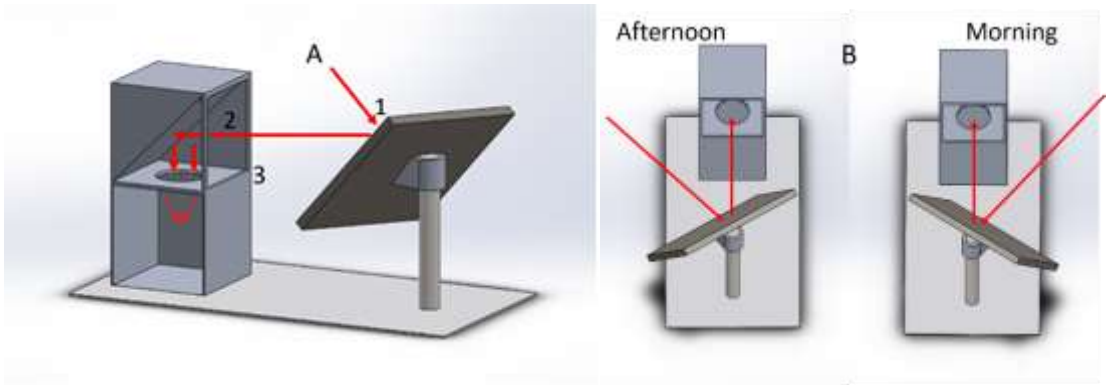

Figure 5: Schematic of solar system (A) side-on and (B) from above

Based on the testing of a laboratory scale design [22], a pilot scale system was built with a final aperture (reflection from secondary mirror) of 1m x 1m. For operation throughout the year the height and width of the primary mirror are 1.5 m and 2.0 m respectively, ensuring full coverage of the secondary mirror even in winter. The control system uses a dual axis slew drive, commonly used for the tracking of photovoltaic panels. The tracking system employs an estimate of the sun's position based on the location and time of day to do the initial positioning. Once established, four light dependent resistors (LDRs) are used to further align the mirror ensuring an even flux level across the aperture. The LDRs are located at the 3, 6, 9 and 12 o'clock positions of the final aperture. The entire system is powered using an

untracked, 80W photovoltaic panel, located on the North side of the secondary mirror enclosure. Thus it has no external power requirements. A 5 A charge controller and a 12 V, 21 Ah lead acid battery is used for storage. The actuators are controlled using custom code on a Raspberry PI microcontroller. The operational unit is displayed in Figure 6.

Figure 6: Pilot scale solar tracking system

A Fresnel lens with a diameter of 470 mm and a focal length of 460 mm was used (Stock #46-392, Edmund Optics, UK). As mentioned, the lens is placed at position 3 in Figure 5A. With this arrangement, naturally collimated sunlight is continuously directed onto the lens, which creates a fixed focal point in space. Thus, the configuration is suitable for use in combination with the moving platform design shown in Figure 4B. The printer platform was constructed from low cost pine wood to have a bed size of 320 mm by 245 mm. An Arduino Mega R3 was used in conjunction with two TB6600 stepper motor drivers to control two NEMA 17 stepper motors. The stepper motor drivers are capable of delivering up to 4 A each, while the stepper motors have a holding torque of 4000 g.cm. Control of the x-direction movement was actuated through a rail, while control of the y-direction was actuated using a threaded rod, schematically illustrated in Figure 7.

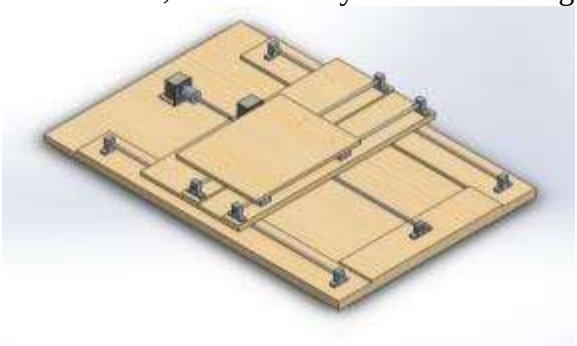

Figure 7: CAD drawing of printer platform design

The rail results in a movement of 40 mm per revolution of the stepper motor, while the threaded rod realizes a movement of 8 mm per revolution of the motor. This makes the rod significantly more accurate; however, the accuracy of the rail was sufficient for the planned

exploratory testing. Because the stepper motors have no means of determining position, homing switches were installed to determine the position of the bed upon start-up. Small misalignments can have a large effect on the spot size, thus it is important to vertically align the printer precisely to the light source. For this reason, it was decided to suspend the printer within the concentrating platform using 4 threaded rods. These can be adjusted to fine-tune the final alignment. The constructed printer, suspended within the platform, is presented in Figure 8.

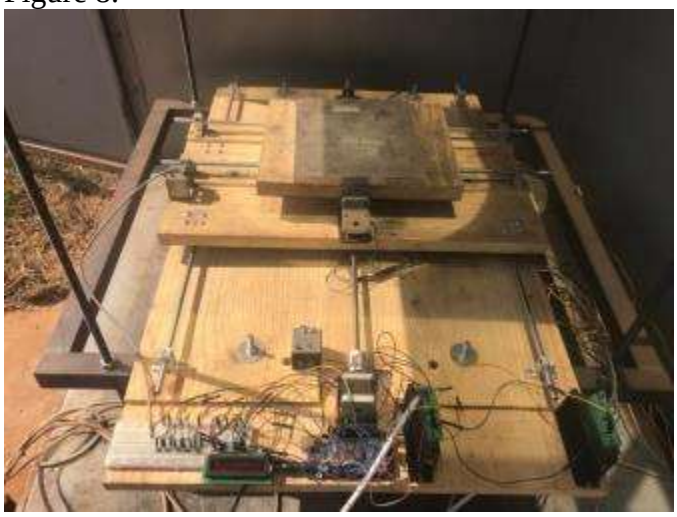

Figure 8: As constructed printer platform

This design is suitable for preliminary testing to determine the overall feasibility of the concept and to establish the basic operating parameters for future devices. However, the platform is only capable of two-dimensional movements and thus only single layered artefacts can be produced. Nonetheless, it is possible to fit a container to the current platform. The container base can be actuated to enable movement in the z-direction. Following the initial sintering the container base can be lowered and an additional layer of powder can be introduced. In this way a three-dimensional object can be constructed. However, the weight of the final powder bed will be limited by the capabilities of the motors driving the platform.

3. Modelling of the sinter/melt process

It is known that a large number of factors affect the SLS process [23]. While a similar number of factors can be expected to influence the solar version of this process, the natural fluctuations of ambient conditions as well as the variable incident radiation increase its complexity. This necessitates the development of an accurate descriptive model. Modelling of the SLS process has been largely focussed on the process of laser sintering of metals [5, 24-26]; however, the sintering of polymers [27] and even of ceramics [28] has been considered. Because of the complex, transient nature of this process, detailed simulations of the distributions of various output parameters utilising numerical methods are common [25, 29, 30]. Analytical expressions for the total imparted energy [5] and a dimensional analysis of the process [23] have also been developed. In order to accurately model the process, key parameters for the powder bed have been identified [25, 31]. Thorough descriptions of the problems potentially affecting the process can be found in literature. The phenomenon known as ‘balling’ [25, 30, 32, 33] is the formation of liquid droplets which reduce the ability of successive layers to adequately bond. The kinetics of incomplete densification [31, 34] have also been modelled. The objective for this investigation was only to provide a simplistic description of the process to act as the basis for future, in-depth investigations.

From a basic analysis of the process it is possible to set up a rudimentary energy balance. As the laser or concentrated solar beam scans across the material it will heat up the powder. The track left by this is known as the *scan vector*. The *hatch-spacing* is the distance between the centres of two adjacent, parallel tracks. This is a critical parameter to ensure that minimal overlap occurs between scans while still ensuring that the tracks are bound together to make a coherently linked structure. Considering an element of the bed equal in size to the irradiated area, the conservation of energy may be expressed as:

$$\dot{Q}_{radiation} = \dot{Q}_{sensible\ heat} + \dot{Q}_{latent\ heat} + \dot{Q}_{lost} \quad (1)$$

Where $\dot{Q}_{lost}$ includes the convective loss and any heat conducted through the base of the bed (assumed negligible). The volume of material heated within a given time period is approximately given by the velocity of the beam (v) multiplied by the layer thickness (L_t) and the focal spot diameter (d), i.e. track width. A portion of the incident radiation is reflected; thus, the equation can be rewritten as [35]:

$$aP = \rho(vdL_t)C_P(T_m - T_\infty) + \rho(vdL_t)\lambda + hd^2(T_m - T_\infty) \quad (2)$$

Where a is the absorptance of the material and P is total power of the incident irradiation. The convective heat transfer coefficient (h) can be calculated using correlations for natural convection. However, this term is several orders of magnitude lower than the others and can be disregarded.

The Buckingham Pi theorem is the core of dimensional analyses. The theorem is given as [36]:
If an equation in n arguments is dimensionally homogeneous with respect to m fundamental units, it can be expressed as a relation between n – m independent dimensionless arguments.

This can also be summed up mathematically, where an output variable, y, is correlated to a number of input variables, x, through a function, f, as:

$$y = f(x_1, x_2, x_3, \dots, x_n) \quad (3)$$

The corresponding dimensionless variable π_y is then described by the equation:

$$\pi_y = F(\pi_1, \pi_2, \pi_3, \dots, \pi_{n-m}) \quad (4)$$

This has the potential to significantly reduce the intricacy of the problem through a reduction in complexity of the expression F when compared to f. The individual dimensionless parameters also have the potential to aid in the understanding of the system. Based on the rudimentary model, the variables affecting the current process can be split into three groups:

1) variables that pertain to the incident irradiation
2) variables that pertain to the material used
3) variables pertaining to the printing process

Variables from group 1 can only be measured, not controlled, i.e. irradiance. Variables from group 2 can only be changed by changing the material, thus during the process they remain fixed. Only the last group contains variables that can be adjusted during the process itself to control certain outcomes. Using the proposed simplistic model, the dimensional analysis was conducted using the following key variables: the latent heat of fusion (λ), the focal spot diameter (d), the absorbed power (aP), the bulk density of the powder (ρ), the scanning velocity (v), the thermal diffusivity (α), the hatch-spacing (H_S), the layer thickness (L_t), the heat capacity (C_p) and the difference in temperature between ambient conditions and the melting point of the polymer $\Delta T = (T_m - T_\infty)$.

The corresponding fundamental dimensions of the problem are therefore: time, distance, mass and temperature. The Pawlowski matrix transformation provides a simpler alternative method to the often-clumsy Buckingham Pi method [37]. For simplicity, the velocity, the spot size, the incident radiation power and the temperature difference are chosen as repeating variables; leaving the remaining variables as core variables. As the number of original variables (10) is reduced by the number of fundamental dimensions (4), six dimensionless variables are created:

$$\pi_1 = \frac{\lambda}{v^2} \tag{5}$$

$$\pi_2 = \frac{\rho\, v^3\, d^2}{aP} \tag{6}$$

$$\pi_3 = \frac{L_t}{d} \tag{7}$$

$$\pi_4 = \frac{\alpha}{v\, d} \tag{8}$$

$$\pi_5 = \frac{H_S}{d} \tag{9}$$

$$\pi_6 = \frac{C_P\, \Delta T}{v^2} \tag{10}$$

A new dimensionless number, in the form of a model function, can be obtained by multiplying dimensionless numbers by each other. Two model functions are generated in this manner:

$$\pi_7 = \frac{1}{\pi_1\, \pi_2 \pi_3} = \frac{aP}{\rho\, d\, L_t\, v\, \lambda} \tag{11}$$

$$\pi_8 = \frac{1}{\pi_2\, \pi_3 \pi_6} = \frac{aP}{\rho\, d\, L_t\, v\, C_P\, \Delta T} \tag{12}$$

The two model functions only differ marginally. The division of equation 11 is by the latent heat of fusion, as opposed to equation 12 where division is by the heat capacity times the delta temperature. Since all of these variables are approximately constant for a given material, the two dimensionless variables π_7 and π_8 will be constant multiples of each other. For this reason, only π_7 will be used to analyse the system. This dimensionless variable represents the ratio of the absorbed solar energy to the energy needed to melt the material. Thus, it can be considered to be the ratio of incident power to required power and its inverse has been proposed in SLS literature as the "melting efficiency" [23]. One would expect this number to remain roughly constant at a variety of operating conditions, since an increase in one term is compensated for by another. In this form it is very much related to the energy density of the source [5].

By measuring the necessary variables and plotting the model function it can be ascertained if the system functions as expected and that the simplified model is an adequate description. If the value remains constant across a range of operating conditions, it can be concluded that the

printer is operating similarly to SLS. Then measurements of specific parameters can be made as a function of the manipulated variables. These relationships can then be used to determine the operational limits and as design inputs for improving future prints and builds.

4. Experimental

The experimental setup shown in Figure 6 and 8 is located in Pretoria, South Africa (S 25º 45' 2.534"; E 28º 15' 42.011"). The reflected solar radiation incident on the Fresnel lens (Point 3 in Figure 5) was measured using an Apogee MP-200 pyranometer. The pyranometer uses a calibrated silicon-cell photodiode with a specified accuracy of 95 %. Since the printer is placed in an enclosed housing, the influence of diffuse radiation on the measurement is minimal. The position of this measurement negates losses caused by dust and other factors affecting any of the reflective surfaces. Additional optical losses are expected due to absorption by the lens itself and the supplier stated transmittance is 92%. In addition, prior measurements [22] indicate that the impact on the spectral distribution is minimal. A single experiment can be conducted within a few minutes. Given this is very short timeframe, an instantaneous measurement was used. The minimum focal spot size that could be achieved has an average diameter of approximately d = 3 mm. This was measured using a DSLR camera at very low aperture and high shutter speed, as shown in Figure 9.

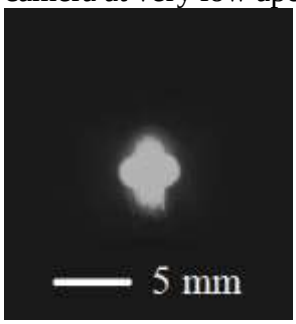

Figure 9: Lens focal spot size

As can be seen from this image the spot is not uniform. The focal point of the lens is affected by the coherence of the light and any manufacturing defects. Using the stipulated values of movement per revolution for each of the stepper motors, the scanning velocity can be fixed within the control program of the platform. The program used to control the motors was custom coded using open source libraries and is included in the Supplementary Material. Samples were created by scanning over a 100 mm by 100 mm square section of the powder bed. The powder utilised was a commercial Nylon 12 SLS powder with a particle size of 40 μm, supplied by Additive Manufacturing Solutions 3D (Pretoria, South Africa). Supplier provided properties are: T_m = 180 ºC, ρ = 1150 kg.m^{-3} and λ = 96.7 kJ.kg^{-1}. The achieved layer thickness after a given print was measured using a sheet-metal micrometer with an accuracy of 0.01 mm. The printed samples were also examined using a Carl Zeiss optical microscope to determine the state of the material.

Initial testing was done to determine the maximum value for the hatch-spacing which resulted in a coherently bonded structure, as assessed by visual inspection and the application of a small force. Once the hatch-spacing was fixed, 25 tests were conducted using different scanning velocities under naturally varying irradiation conditions. Full details of each test result are provided in Appendix A. A further four tests were conducted using the nitrate based solar salt. A eutectic mixture of $NaNO_3$ and KNO_3 (~50/50 mass %) was previously

characterized [38], to have properties of: T_m = 222 ºC, ρ = 1500 kg.m^{-3} and λ = 117 kJ.kg^{-1}. The salt provides additional validation of the model function.

5. Results and Discussion

The hatch-spacing was first set at 6 mm and a scan was done at 45 mm.s^{-1} with the result shown in Figure 10 A. As can be seen from this image, the tracks are not physically bound together and the application of a small force is enough to pull the structure apart. When the hatch-spacing is decreased to 4 mm, it is no longer possible to disintegrate the structure by the application of a small force. Thus, the tracks are interlinked, however, as can be seen from Figure 10 B there is still significant light penetration through the structure. At a hatch-spacing of 2 mm of fully coherent structure is achieved with considerable tensile strength and little light penetration, as visible from Figure 10 C. The results could have been anticipated since a hatch-spacing larger than the focal spot size of 3 mm, implies that areas outside of the spot region are only heated through conduction. However, the spot diameter is not completely uniform. Hence a final hatch-spacing of 2 mm was chosen to ensure good bonding but avoid excessive track overlap.

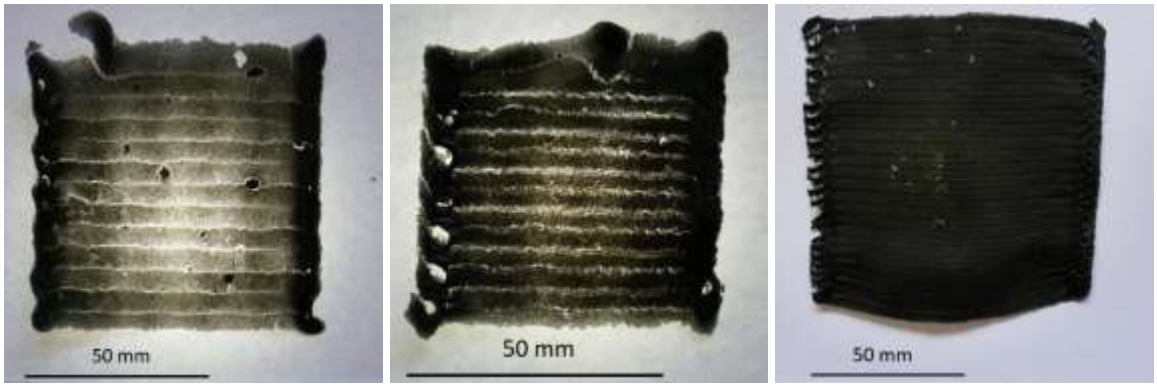

Figure 10: A B C Hatch-spacing of 6, 4 and 2 mm

The scanning velocity was adjusted from 25 to 80 mm.s^{-1} under variable irradiation conditions. The results of all the nylon tests are used to calculate 25 values of the incoming power to required power ratio, or dimensionless variable π_7. For the purposes of this preliminary assessment the absorptance is set to one. These values are plotted against the scan speed in Figure 11.

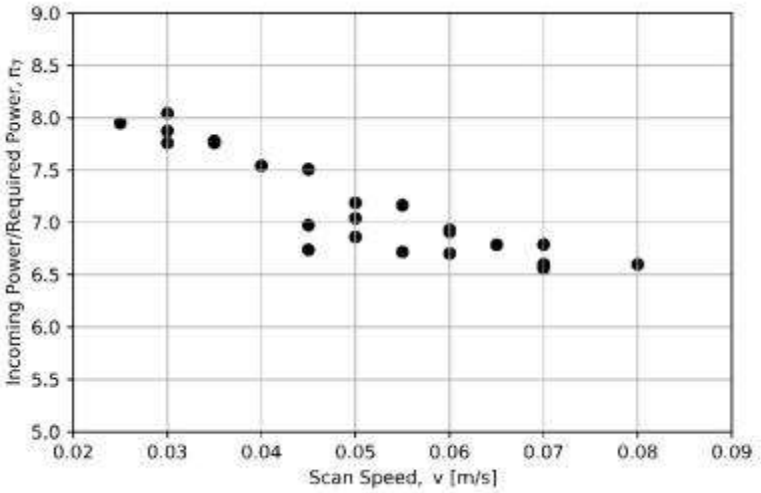

Figure 11: Dimensionless Power Ratio vs Scan Speed

While this appears to be a rough trend, it actually represents two distinct regions. The indication is that when the scan speed is increased, a reduction in the power ratio is evident. This is in contradiction with the expectation from the modelling, where it is presumed that a slower scan rate will simply result in a thicker layer. This indicates that an additional effect is taking place. The samples were examined using an optical microscope to determine the cause. Based on this it was possible to classify the samples into two different categories: samples that had only sintered and samples that had both sintered and melted. Figure 12 displays a sample which has undergone both sintering and melting.

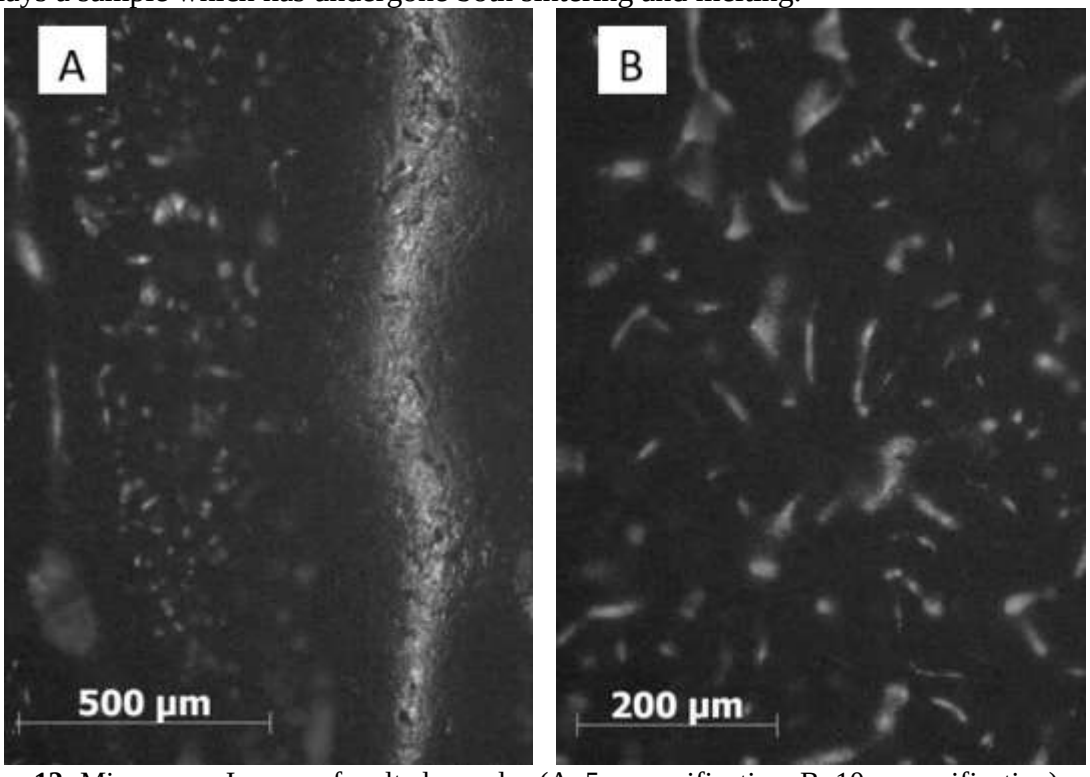

Figure 12: Microscope Images of melted samples (A: 5x magnification, B: 10x magnification)

At low magnification (5x) it is possible to distinguish between regions with varying degrees of particle coalescence. The melt track is clearly visible in the figure, indicating the presence of strong coalescence of the molten particles. The molten region appears at the centre of a

scan vector, at the location where the intensity of radiation is expected to be at a maximum. Sintering is visible on the sides of the melt track. This is due to heat conducted laterally from the beam as well as some level of stray radiation. The unavoidable spread in intensity is due to the light not being perfectly collimated and manufacturing defects in the lens. An example of a sample that has only undergone sintering is shown in Figure 13.

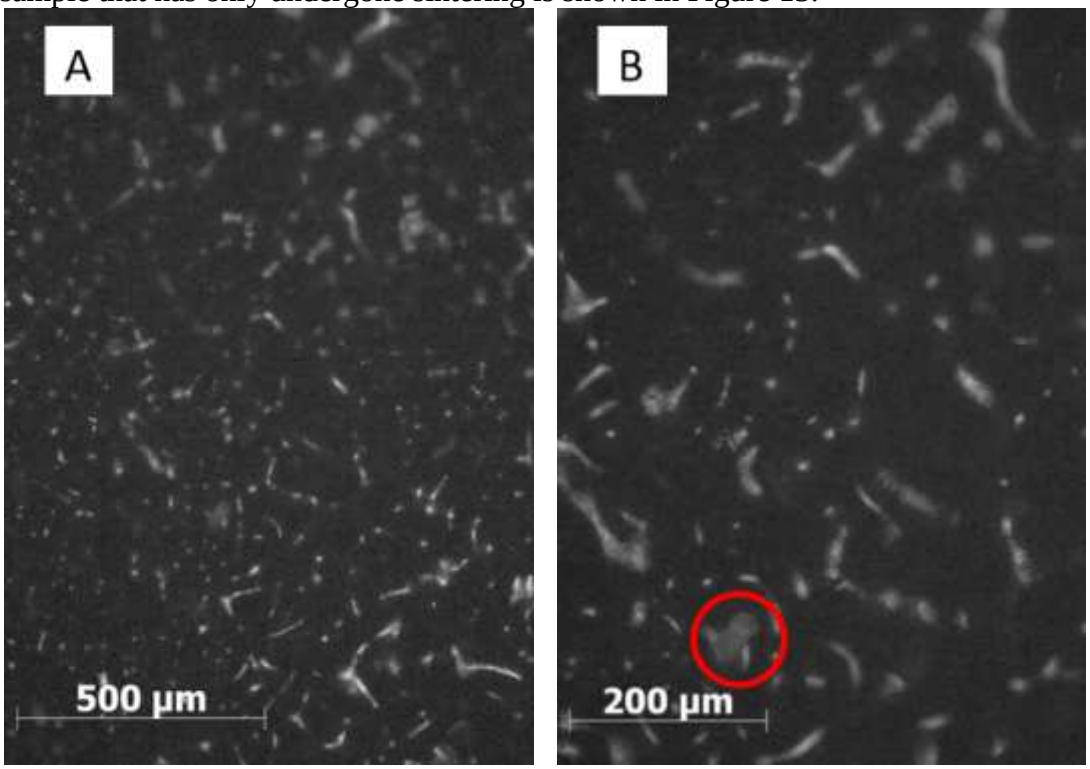

Figure 13: Microscope Images of sintered samples (A: 5 times magnification, B: 10 times magnification)

Individual grains are unmistakeably distinguishable, but a degree of coalescence is evident. At higher magnification (10x) this effect is clearer but some individual, unsintered particles can also be found (encircled in Figure 13). Thus, it is evident that the exhibited sample has only undergone sintering via the solid-state sintering process. The test data is replotted in Figure 14, with each sample classified as only sintered or sintered and melted.

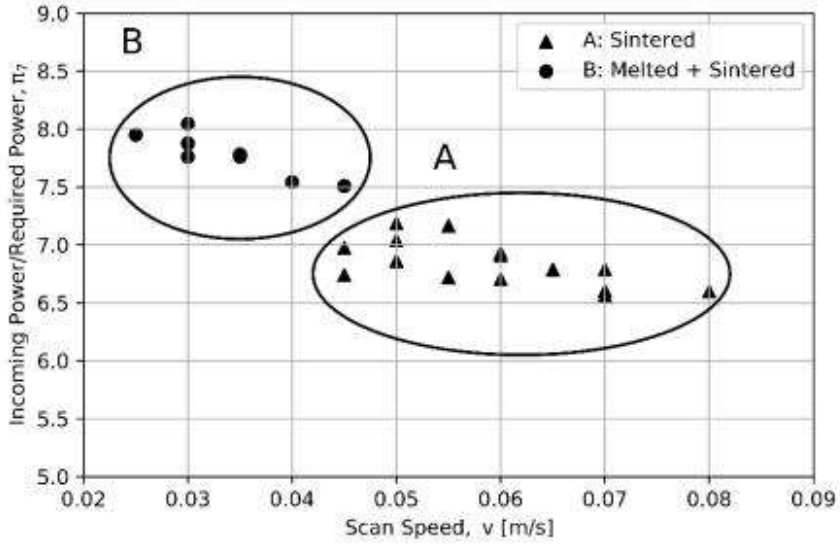

Figure 14: Classified dimensionless Power Ratio vs Scan Speed

Now it is clear that as the scan speed is increased a discrete transition occurs between melting and sintering. This is sensible as the time available to absorb the radiation is reduced, leading to less coalescent melting and transitioning into pure sintering. Since the power requirements for these two transitions are different, it is to be expected that they should have different values of the dimensionless variable π_7. This is confirmed by the average values for the two different categories. The mean of the sintered samples is 6.84 with a variance of 0.04, while the mean for the samples that had both sintered and melted is 7.75 with a variance of 0.03. Given the fact that the distinction between the samples were made based on visual inspection alone, the variance is low and a statistically significant decrease of 12% is evident for the transition from melting to sintering. A degree of overlap in terms of speed is seen between the datasets, indicating that the scan speed is not the sole factor in determining whether a sample undergoes only sintering or both sintering and melting.

To further substantiate the validity of the dimensionless number for sintering, the tests were repeated using a solar salt. A small amount of carbon black was added to the salt to achieve a similar absorptance to the black Nylon 12. The tests were conducted at scan rates which ensured only sintering was taking place, as verified by inspection with the microscope. The mean value achieved for the salt was 7.06 which is within 3% of the value obtained for Nylon 12. This supports the assertion that if a single transformation process is taking place, i.e. only sintering, the model function is a sufficient description of the process.

Since the model function has been shown to be consistent with expectations, it implies that the key parameters for the operation of the unit have been captured. This means it is possible to use the data to relate specific parameters to manipulated variables and potential disturbances. This will demonstrate the limitations of the current design and enable better control. A relation of specific interest is the dependence of the layer thickness on the scan speed under the influence of varying solar flux levels. Based on equation 11 the layer thickness should be directly proportional to the ratio of the irradiance and the scanning velocity. The correlation is clearly illustrated by Figure 15 for all the nylon data.

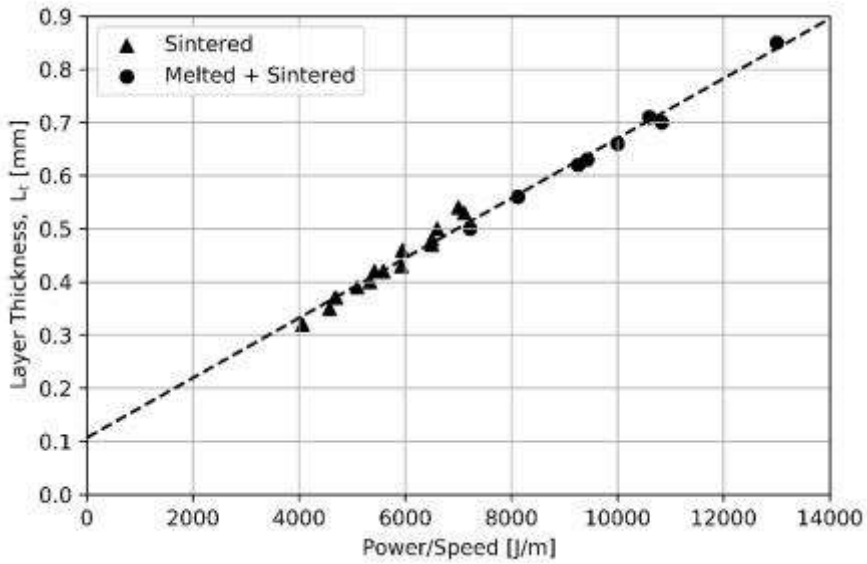

Figure 15: Layer Thickness vs Power to Speed Ratio

While the exact flux incident on the material was not measured, the trend in Figure 15 indicates that variations in the radiant power have been suitably captured. If not, it is

expected that this data would have exhibited substantial scatter. The linear trend can be described by the following equation with a coefficient of fit for this correlation is 0.989:

$$L_t = \ 5.63 \times 10^{-5} \left(\frac{P}{v}\right) + 0.107 \qquad (13)$$

Thus, there is a direct relationship between the scanning velocity and the achieved layer thickness. This result indicates that it will be fairly straightforward to control the layer thickness during long prints where the solar flux will unavoidably be subject to natural variations over time. A feedforward system can use a digital measurement of the irradiation to dynamically compensate the scanning velocity, thereby resulting in an even thickness. This adjustment would be proportional to the variation and thus does not require a highly accurate absolute measurement of the irradiation. The figure also provides additional information regarding the limitations of the current design. Below a power/speed ratio of around 4000 $J.m^{-1}$, the structural integrity of the printed layer is compromised. The layer is too thin to withstand even the smallest applied force. On the other hand, thermal degradation of the polymer occurs beyond ratios of approximately 14 000 $J{\cdot}m^{-1}$. These two effects are demonstrated in Figure 16 A and B respectively.

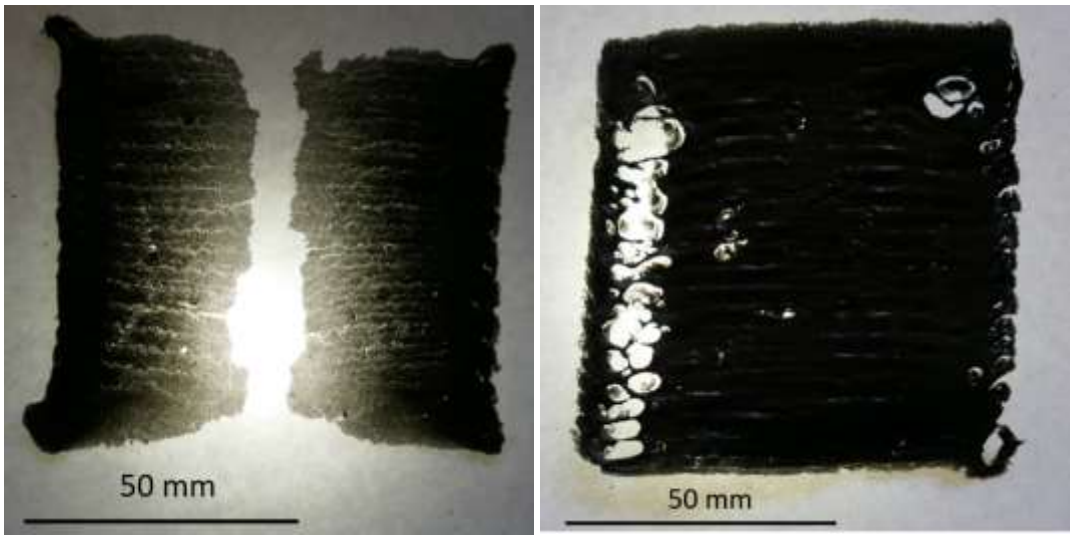

Figure 16: A Structural integrity loss and B thermal degradation

This bounds the achievable layer thickness to between 0.3 and 0.9 mm for the current configuration. The limits are related to the material properties such as particle size and thermal diffusivity, as well as the device operation. Thus, these values can be improved in future builds or by selecting different powders. The results have demonstrated that it is possible to selectively solar sinter a typical SLS material. For pure sintering a readily achievable layer thickness is around 0.3 mm, which is comparable to SLS at around 0.1 - 0.15 mm [39]. The achieved hatch-spacing of 2 mm is however significantly higher when compared to SLS at 0.15 - 0.3 mm [39]. This is a direct consequence of the achieved focal spot size. If a cast glass lens is used a smaller spot size can be achieved since some of the limitations of using a Fresnel design are overcome. A detailed image of the printed sample is shown in Figure 17

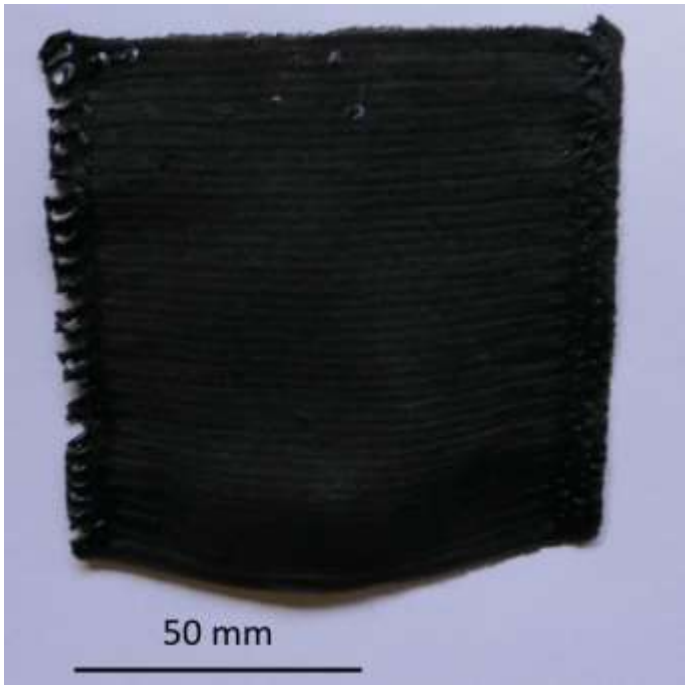

Figure 17: Sintered Polymer Sample

Some flaws are evident, for example the sample texture is uneven. This in turn results in warping. Such defects are not uncommon in 3D printed objects where the printing methodology has not been suitably optimized. The uneven texture is due to the scanning strategy of the printer, which slows down to a standstill at the end of a scan vector, before repositioning the bed according to the hatch-spacing and then starting a new vector. These issues can be corrected by developing a printing procedure that is customized to the solar sintering process. From an efficiency perspective, the design could also be improved. The incident normal radiation on the primary mirror (DNI) varied between 850 – 900 $W.m^{-2}$, as measured by the Southern African Universities Radiometric Network [40]. The average radiation incident on the Fresnel lens listed in Table 1 is approximately 330 $W.m^{-2}$. This places the optical path efficiency before the lens (Point 1 to 3 in Figure 5) at around 40%. This low value is due to the low-cost mirrors utilized (large diffuse reflectance component) as well as the build-up of dust and damage over time.

The dimensionless variable π_7 gives an indication of the efficiency of the remaining portion of the device. The ratio of incoming power (measured above the Fresnel lens) to the theoretical power required to melt the Nylon 12 (region B, Figure 14), indicates approximately 7.75 times more energy is supplied than needed. The absorptivities of black plastic materials are generally quite high (>90%) [35, 41]. However the thin powder bed is porous which will lead to increased transmittance compared to a solid plastic. Using a value for woven plastic nets as a guide [42, 43] this may be estimated at around 70% for a black porous bed. The lens transmittance is 92% which means 83% of the oversupply is lost to the lens absorption and surface transmittance or scattering. This gives an overall efficiency of $1/(7.75*0.92*0.7)*100\% \approx 20\%$.

The remaining heat losses are conductive and reflective. Since the material is porous and the support is wood, it is unlikely that conductive losses are substantial. Thus a large portion of the available energy is lost to convection. The energy source is sunlight and since the efficiency does not impact on the printing resolution, it does not influence the printed article cost. However, the achievable temperature will be limited by the stated efficiency. If higher

melting components are to be sintered the system must be redesigned to limit convective losses and improve the optical efficiency of the mirror system. Finally, it should be noted that it was assumed that the irradiation is homogenous across the estimated focal point diameter of 3mm. In reality the situation is significantly more complex and the true spot size achieved is determined by the optical properties of the lens and the specific material used. Thus the measurements presented in Table 1 are limited to the current system only and are not generally valid.

6. Conclusions and Recommendations

The high cost and power requirements of machines capable of producing complex parts from a range of powdered precursor materials have restricted their widespread use. As an alternative to these methods, selective sintering through the use of concentrated solar power has been tested. The total cost of the proposed system was around $ 1,000, using inexpensive, "off-the-shelf" components. Commercial SLS printers sell from $10,000 up to $250,000 depending on the size of the printed component. The approach would have the additional benefit of making the additive manufacturing process completely sustainable, allowing entrepreneurs and microbusinesses off-grid access to additive manufacturing techniques. No prior data exists on the use of selective solar sintering, thus it was necessary to design and construct a prototype for preliminary feasibility testing. Future work will focus on investigating the optimal trade-off between the low system cost and the consequently low efficiency.

To perform tests required for the modelling of the process, a Fresnel lens was used to concentrate sunlight has been built. Light is directed for this procedure through the integration of the power tower concept with a secondary mirror to provide a constant source of solar irradiation for the lens. Two dimensional samples were created at varying incident radiations and scanning velocities to develop a suitable model. Parameters for this model were condensed to the most significant combinations through application of a dimensional analysis. The most important of these is a ratio of the incoming power of the solar radiation to the power required to sinter or melt the particle.

To create suitable samples the effect of the hatch-spacing on the structural integrity of the sample was first tested. It was determined that an optimal hatch-spacing for this procedure has a magnitude slightly smaller than the spot size of the lens. This allows the material of adjacent scan vectors to be adequately bonded while limiting track overlap. A distinction in the testing data was made between samples in which only sintering was observed and samples which had both sintered and melted. The dimensionless model function was found to be constant using both Nylon 12 and solar salt. This validated the assertion that the model adequately captured the relevant parameters of the process.

An important relation was developed, namely the dependence of the layer thickness on measurable input conditions— the incident radiation— and controllable process conditions— the scan speed. The linear dependence of the layer thickness on the ratio of irradiance to scanning velocity was confirmed. This indicates the layer thickness will be controllable by measuring the incoming radiation. Limiting conditions for the achievable layer thickness were found to be between 0.3 mm and 0.9 mm, with the minimum in the same order of magnitude as current SLS approaches (~0.1 mm). However, the current methods still trail conventional SLS methods in terms of achievable resolution. This is due to the Fresnel lens

currently employed which only achieves a rough spot size of 3 mm. This can be improved through the use of cast glass lenses which suffer less from manufacturing defects.

The current testing only involved 2D sheets and it was noted that if the powder bed was to incorporate movement in the z-direction, its weight would require substantially more costly drive motors. However, given the progress achieved through the current design an alternative configuration has become evident which overcomes this limitation. If the aperture of the optical system is enlarged to extend beyond the edge of the powder bed by half of the lens diameter, the lens focal point can be moved anywhere over the bed and still be fully covered by collimated solar irradiation. Thus it would be possible to have a stationary bed using a positioning mechanism for the lens, which is comparatively light weight. Essentially the system would operate in the same fashion as conventional SLS systems. Since the bed is stationary 3D object production would be straightforward. The implication is that the aperture is substantially larger than the lens, hence some of the sunlight is wasted. However, since the utilised slew drive motors can handle higher weight loadings, increasing the size of the mirrors will only result in a minor increase in the overall cost. This configuration will be the subject of planned testing. In addition, future work will look also look at feedforward control and generalizing the measured operating parameters beyond the current lens and material combination.

7. References

[1] Zhu, J.H., Zhang, W.H. and Xia, L., 2016. Topology optimization in aircraft and aerospace structures design. Archives of Computational Methods in Engineering, 23(4), pp.595-622.

[2] Tomlin, M. and Meyer, J., 2011, May. Topology optimization of an additive layer manufactured (ALM) aerospace part. In Proceeding of the 7th Altair CAE technology conference (pp. 1-9).

[3] Huang, S. H., Liu, P., Mokasdar, A., & Hou, L. (2013). Additive manufacturing and its societal impact: A literature review. *International Journal of Advanced Manufacturing Technology*, *67*(5–8), 1191–1203.

[4] Feng, L.Y., 2014. Study on the status quo and problems of 3D printed buildings in China. Global Journal of Human-Social Science Research, 14(5).

[5] Simchi, A. (2006). Direct laser sintering of metal powders: Mechanism, kinetics and microstructural features. *Materials Science and Engineering A, 428,* 148-158.

[6] Santos, E., Osakada, K., Shiomi, M., Morita, M. and Abe, F., 2004, October. Fabrication of titanium dental implants by selective laser melting. In Fifth International Symposium on Laser Precision Microfabrication (Vol. 5662, pp. 268-274). International Society for Optics and Photonics.

[7] Abe, F., Osakada, K., Shiomi, M., Uematsu, K. and Matsumoto, M., 2001. The manufacturing of hard tools from metallic powders by selective laser melting. Journal of materials processing technology, 111(1-3), pp.210-213.

[8] Buchbinder, D., Schleifenbaum, H.B., Heidrich, S., Meiners, W. and Bültmann, J., 2011. High power selective laser melting (HP SLM) of aluminum parts. Physics Procedia, 12, pp.271-278.

[9] Zhang, H.L., Baeyens, J., Degrève, J. and Cacères, G., 2013. Concentrated solar power plants: Review and design methodology. Renewable and sustainable energy reviews, 22, pp.466-481.

[10] Baharoon, D.A., Rahman, H.A., Omar, W.Z.W. and Fadhl, S.O., 2015. Historical development of concentrating solar power technologies to generate clean electricity

efficiently–A review. Renewable and Sustainable Energy Reviews, 41, pp.996-1027.
[11] Lovegrove, K., Burgess, G. and Pye, J., 2011. A new 500 m2 paraboloidal dish solar concentrator. Solar Energy, 85(4), pp.620-626.
[12] Xie, W.T., Dai, Y.J., Wang, R.Z. and Sumathy, K., 2011. Concentrated solar energy applications using Fresnel lenses: A review. Renewable and Sustainable Energy Reviews, 15(6), pp.2588-2606.
[13] Andreev, V.M., Vlasov, A.S., Khvostikov, V.P., Khvostikova, O.A., Gazaryan, P.Y., Sadchikov, N.A. and Rumyantsev, V.D., 2006, May. Solar thermophotovoltaic converter with Fresnel lens and GaSb cells. In Photovoltaic Energy Conversion, Conference Record of the 2006 IEEE 4th World Conference on (Vol. 1, pp. 644-647). IEEE.
[14] Sierra, C. and Vazquez, A.J., 2006. NiAl coating on carbon steel with an intermediate Ni gradient layer. Surface and Coatings Technology, 200(14-15), pp.4383-4388.
[15] Rietema, M.J., 2013. Design of a solar sand printer.
[16] Neumann, F. and Curbach, M. 2016 Method and apparatus for thermal treatment of the sand. German Patent DE102015112282A1
[17] Kayser, M., 2011. Solar Sinter Project. Markus Kayser.
[18] Wu, Y., Connelly, K., Liu, Y., Gu, X., Gao, Y. and Chen, G.Z., 2016. Smart solar concentrators for building integrated photovoltaic façades. Solar Energy, 133, pp.111-118.
[19] Lifante, G., Cusso, F., Meseguer, F. and Jaque, F., 1983. Solar concentrators using total internal reflection. Applied optics, 22(24), pp.3966-3970.
[20] García, H., Ramírez, C. and León, N., 2014. Innovative solar tracking concept by rotating prism array. International Journal of Photoenergy, 2014.
[21] Feuermann, D., Gordon, J.M. and Huleihil, M., 2002. Solar fiber-optic mini-dish concentrators: first experimental results and field experience. Solar Energy, 72(6), pp.459-472.
[22] Badenhorst, H., Fox, N. and Mutalib, A., 2016. The use of graphite foams for simultaneous collection and storage of concentrated solar energy. Carbon, 99, pp.17-25.
[23] van Elsen, M., Al-Bender, F. & Kruth, J.P. (2008). Application of dimensional analysis to selective laser melting. *Rapid Prototyping Journal, 14(1)*, 15-22
[24] Wang, X. C., Laoui, T., Bonse, J., Kruth, J. P., Lauwers, B., & Froyen, L. (2002). Direct Selective Laser Sintering of Hard Metal Powders : Experimental Study and Simulation. *International Journal of Advanced Manufacturing Technology*, *19*, 351–357.
[25] Tolochko, N. K., Arshinov, M. K., Gusarov, A. V., Titov, V. I., Laoui, T., & Froyen, L. (2003). Mechanisms of selective laser sintering and heat transfer in Ti powder. *Rapid Prototyping Journal*, *9*(5), 314–326.
[26] Fischer, P., Locher, M., Romano, V., Weber, H. P., Kolossov, S., & Glardon, R. (2004). Temperature measurements during selective laser sintering of titanium powder. *International Journal of Machine Tools and Manufacture*, *44*(12–13), 1293–1296.
[27] Childs, T. H. C., Berzins, M., Ryder, G. R., & Tontowi, A. (1999). Selective laser sintering of an amorphous polymer—simulations and experiments. *Proceedings of the Institution of Mechanical Engineers, Part B: Journal of Engineering Manufacture*, *213*(4), 333–349
[28] Bertrand, P., Bayle, F., Combe, C., Goeuriot, P., & Smurov, I. (2007). Ceramic components manufacturing by selective laser sintering. *Applied Surface Science*, *254*(4), 989–992.
[29] Bugeda, M., Cervera, G., & Lombera, G. (1999). Numerical prediction of temperature and density distributions in selective laser sintering processes. *Rapid Prototyping Journal*, *5*(1), 21–26.
[30] Gusarov, A. V., Yadroitsev, I., Bertrand, P., & Smurov, I. (2007). Heat transfer modelling and stability analysis of selective laser melting. *Applied Surface Science*,

254(4), 975–979.
[31] Gusarov, A. V., Laoui, T., Froyen, L., & Titov, V. I. (2003). Contact thermal conductivity of a powder bed in selective laser sintering. *International Journal of Heat and Mass Transfer*, *46*(6), 1103–1109.
[32] Yap, C. Y., Chua, C. K., Dong, Z. L., Liu, Z. H., Zhang, D. Q., Loh, L. E., & Sing, S. L. (2015). Review of selective laser melting: Materials and applications. *Applied Physics Reviews*, *2*(4).
[33] Agarwala, M., Bourell, D., Beaman, J., Marcus, H., & Barlow, J. (1995). Direct selective laser sintering of metals. *Rapid Prototyping Journal*, *1*(1), 26–36.
[34] Kruth, J. P., Wang, X., Laoui, T., & Froyen, L. (2003). Lasers and materials in selective laser sintering. *Assembly Automation*, *23*(4), 357–371
[35] Bergman, T.L., Incropera, F.P., DeWitt, D.P. and Lavine, A.S., 2011. Fundamentals of heat and mass transfer. John Wiley & Sons.
[36] Brand, L. (1957). The Pi Theorem of Dimensional Analysis. *Archive for Rational Mechanics and Analysis*, *1*(1), 35–45.
[37] Osswald, T. A. (2015). *Understanding Polymer Processing: Processes and Governing Equations*. Carl Hanser Verlag GmbH & Company KG.
[38] Badenhorst, H. and Böhmer, T., (2018). Enthalpy of fusion prediction for the economic optimisation of salt based latent heat thermal energy stores. *Journal of Energy Storage*, 20, pp.459-472.
[39] Zarringhalam, H., Hopkinson, N., Kamperman, N.F. and De Vlieger, J.J., (2006). Effects of processing on microstructure and properties of SLS Nylon 12. *Materials Science and Engineering*: A, 435, pp.172-180.
[40] Brooks, M.J., Du Clou, S., Van Niekerk, W.L., Gauché, P., Leonard, C., Mouzouris, M.J., Meyer, R., Van der Westhuizen, N., Van Dyk, E.E. and Vorster, F.J., 2015. SAURAN: A new resource for solar radiometric data in Southern Africa. Journal of energy in Southern Africa, 26(1), pp.2-10.
[41] Wolfe, W.L. ed., 1995. Handbook of optics (Vol. 2, pp. 33-66). New York: McGraw-Hill.
[42] Abdel-Ghany, A.M., Al-Helal, I.M. and Shady, M.R., 2015. On the emissivity and absorptivity of plastic shading nets under natural conditions. Advances in Mechanical Engineering, 7(1), p.165605.
[43] Birkebak, R.C., Hartnett, J.P. and Eckert, E.R.G., 1962. Measurement of radiation properties of solid materials. In Progress in International Research on Thermodynamic and Transport Properties (pp. 563-574).

Appendix A: Test Results

Table 1: Test Raw Data

I [W/m2]	v [mm/s]	L_t [mm]	d [mm]	ρ[kg/m3]	Melted	λ [J/kg]	π_7
325.00	25.00	0.85	3.00	1150.00	1	96700	7.95
325.00	30.00	0.70	3.00	1150.00	1	96700	8.05
318.00	30.00	0.71	3.00	1150.00	1	96700	7.76
300.00	30.00	0.66	3.00	1150.00	1	96700	7.88
330.00	35.00	0.63	3.00	1150.00	1	96700	7.78
324.00	35.00	0.62	3.00	1150.00	1	96700	7.76
330.00	35.00	0.63	3.00	1150.00	1	96700	7.78
325.00	40.00	0.56	3.00	1150.00	1	96700	7.54
325.00	40.00	0.56	3.00	1150.00	1	96700	7.54
320.00	45.00	0.53	3.00	1150.00	0	96700	6.98
315.00	45.00	0.54	3.00	1150.00	0	96700	6.74
325.00	45.00	0.50	3.00	1150.00	1	96700	7.51
325.00	50.00	0.47	3.00	1150.00	0	96700	7.19
330.00	50.00	0.50	3.00	1150.00	0	96700	6.86
325.00	50.00	0.48	3.00	1150.00	0	96700	7.04
326.00	55.00	0.43	3.00	1150.00	0	96700	7.17
327.00	55.00	0.46	3.00	1150.00	0	96700	6.72
320.00	60.00	0.40	3.00	1150.00	0	96700	6.93
335.00	60.00	0.42	3.00	1150.00	0	96700	6.91
325.00	60.00	0.42	3.00	1150.00	0	96700	6.71
331.00	65.00	0.39	3.00	1150.00	0	96700	6.79
329.00	70.00	0.37	3.00	1150.00	0	96700	6.61
320.00	70.00	0.35	3.00	1150.00	0	96700	6.79
327.00	70.00	0.37	3.00	1150.00	0	96700	6.57
325.00	80.00	0.32	3.00	1150.00	0	96700	6.60
332.00	29.00	0.55	3.00	1500.00	0	117000	6.86
349.00	31.00	0.52	3.00	1500.00	0	117000	7.13
354.00	34.00	0.47	3.00	1500.00	0	117000	7.30
407.00	30.00	0.64	3.00	1500.00	0	117000	6.99